nature portfolio

https://doi.org/10.1038/s41586-022-05031-2

Supplementary information

Heterodimensional superlattice with in-plane anomalous Hall effect

In the format provided by the authors and unedited

Supplementary Information

Heterodimensional superlattice with in-plane anomalous Hall effect

Jiadong Zhou[1#]*, Wenjie Zhang[2,3#], Yung-Chang Lin[4#], Jin Cao[1#], Yao Zhou[5,6], Wei Jiang[1], Huifang Du[1], Bijun Tang[5], Jia Shi[7], Bingyan Jiang[2], Xun Cao[5], Bo Lin[5], Qundong Fu[5], Chao Zhu[5], Wei Guo[1], Yizhong Huang[5], Yuan Yao[8], Stuart S. P. Parkin[3], Jianhui Zhou[9], Yanfeng Gao[10], Yeliang Wang[11], Yanglong Hou[12], Yugui Yao[1]*, Kazu Suenaga[4]*, Xiaosong Wu[2]*, Zheng Liu[5,13,14*]

[1]Centre for Quantum Physics, Key Laboratory of Advanced Optoelectronic Quantum Architecture and Measurement (MOE), School of Physics, Beijing Institute of Technology, Beijing 100081, China

[2]State Key Laboratory for Artificial Microstructure and Mesoscopic Physics, Frontiers Science Center for Nano-optoelectronics, and Collaborative Innovation Center of Quantum Matter, Peking University, Beijing 100871, China

[3]Max Planck Institute of Microstructure Physics, Halle 06120, Germany

[4]The Institute of Scientific and Industrial Research, Osaka University, Osaka 567-0047, Japan

[5]School of Materials Science and Engineering, Nanyang Technological University, Singapore 639798, Singapore

[6]Advanced Research Institute of Multidisciplinary Science, and School of Chemistry and Chemical Engineering, Beijing Institute of Technology, Beijing 100081, China

[7]Department of Chemistry, National University of Singapore, 3 Science Drive 3, Singapore 117543

[8]Institute of Physics, Chinese Academy of Sciences, Beijing 100190, China

[9]Anhui Key Laboratory of Condensed Matter Physics at Extreme Conditions, High Magnetic Field Laboratory, HFIPS, Anhui, Chinese Academy of Sciences, Hefei 230031, P.R. China

[10]School of Materials Science and Engineering, Shanghai University, Shanghai 200444, China

[11]School of Integrated Circuits and Electronics, Beijing Institute of Technology, Beijing 100084, P. R. China

[12]Beijing Key Laboratory for Magnetoelectric Materials and Devices, Beijing Innovation Center for Engineering Science and Advanced Technology, School of Materials Science and Engineering, Peking University, Beijing 100871, China

[13] CINTRA CNRS/NTU/THALES, UMI 3288, Research Techno Plaza, Singapore, Singapore

[14]School of Electrical and Electronic Engineering, Nanyang Technological University, Singapore, Singapore

OUTLINE

Section I: Materials preparation and characterization

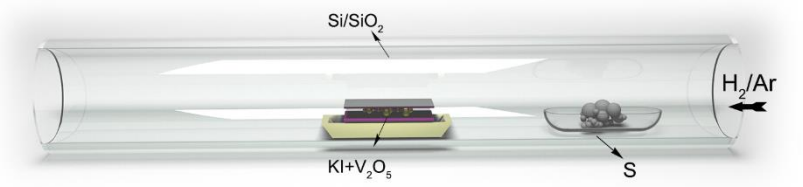

Figure | S1. Reaction setup for synthesis of VS_2-VS superlattices. In our experiment, the mixed powder of KI and V_2O_5 were used as precursors. The H_2/Ar was used as the carrier gas.

To better understand the growth mechanism, different growth conditions and precursors were explored.

1) **Reaction equation and the role of precursors**

The corresponding chemical reactions for VS_2, V_5S_8 and VS_2-VS superlattice can be proposed below:

$$V_2O_5 + 5H_2 + 4S = 2VS_2 + 5H_2O \quad (1)$$

$$10VCl_3 + 17H_2 + 18S = 2V_5S_8 + 2H_2S + 30HCl \quad (2)$$

$$V_2O_5 + 5H_2 + 3S = VS_2\text{-}VS + 5H_2O \quad (3)$$

When the VCl_3 was used as the precursor, the V_5S_8 flake can be obtained, which has been reported before[1].

Compared to the V_5S_8, V_2O_5 was used to synthesize the VS_2 and VS_2-VS superlattice. The differences in the growth conditions between VS_2 and VS_2-VS superlattice are discussed below. First, the formation energy of VS_2 is lower than that of VS_2-VS, resulting in different growing temperatures of both materials. Second, from the chemical reactions (1) and (3), the required amount of sulfur for producing VS_2 and

VS_2-VS superlattice is “4S” and “3S”, respectively. Therefore, reducing sulfur will most likely lead to the formation of VS_2-VS superlattice.

2) Gibbs free energy

The corresponding changes in Gibbs free energy of the (1) and (3) can be written as:

$$\Delta_r G_m(VS_2) = \frac{5}{2}\Delta_f G_m(H_2O \cdot g) + \Delta_f G_m(VS_2 \cdot s) - \frac{5}{2}\Delta_f G_m(H_2 \cdot g) - \frac{1}{2}\Delta_f G_m(V_2O_5 \cdot g) - 2\Delta_f G_m(S \cdot g)$$

$$\Delta_r G_m(VS - VS_2) = 5\Delta_f G_m(H_2O \cdot g) + \Delta_f G_m(VS - VS_2 \cdot s) - 5\Delta_f G_m(H_2 \cdot g) - \Delta_f G_m(V_2O_5 \cdot g) - 3\Delta_f G_m(S \cdot g)$$

These equations also indicate that less sulfur flux is the key to the formation of VS_2-VS. Thus, in our experiment, the sulfur flux was carefully controlled by the pre-heating temperature of sulfur precursor and the growing duration to synthesize the VS_2-VS superlattice.

3) VLS model

In fact, the growth follows a typical VLS mechanism. In our experiment, the growing temperature is higher than 750 ºC. At such a temperature, the KI has become liquid (The melting point is about 680 ºC), and the VLS growing mechanism becomes dominant. This growth mechanism was often observed in nanowire growth[2,3].

4) Controlled experiment

Figure S2 shows the growth mechanism and Fig. S3 shows the as synthesized VS_2 and V_5S_8 using different precursors. In order to let readers repeat the experiment easily, we summarized the growth conditions in Table S1.

Table S1. Summary of the Growth conditions of V_xS_y.

Materials	Growth conditions		
	Metal source	**S flux**	Growth temperature (°C)
VS_2	V_2O_5+KI	More S	700 ~ 730
V_5S_8	VCl_3	Normal S	600
VS_2-VS superlattice	V_2O_5+KI	Less S	750 ~ 800

The 2D-1D superlattice is defined from the atomic structure of the superlattice, in which the structure consists of alternating 2D and 1D structures, different from the traditional superlattice with 0D/2D-2D-or 2D-3D. The comparison of the superlattice obtained via different methods is shown in Table S2.

Table S2. The comparison of the superlattice obtained via different method.

Superlattice structure	0D-2D/3D	2D/3D-2D/3D	1D-2D
Materials	V_5S_8[4], CrTe[5], Cr_2Te_3[6], Cr_3Te_4[7], Cr_4Te_5[8], Cr_5Te_8[8], $NbCr_{1/3}S_2$[9], $Nb_{1+x}S_2$[10],	$(Pb,Sn)_{6+x}Sb_2FeSn_2S_{14+x}$[11], GaAs–AlAs[12], $(Bi_2Se_3)_{12}/(In_2Se_3)_6$[13], GeTe/$Sb_2Te_3$[14], $[(MX)_{1+d}]_m(TX_2)_n$[11,15], NbS_2-Ba_3NbS_5[16]	VS_2-VS
Methods	CVT and CVD	MBE and CVT	Salt assisted CVD

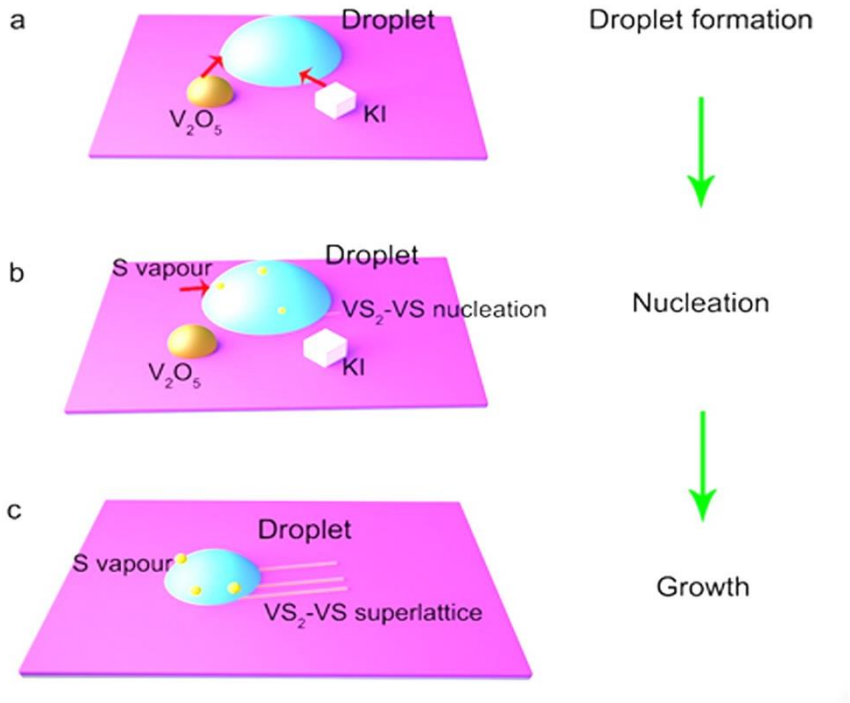

Figure S2 | Growth mechanism of VS_2-VS superlattice. First, droplet was formed between KI and V_2O_5. Then, the VS_2-VS nucleation was formed. Last, the VS_2-VS superlattice was obtained.

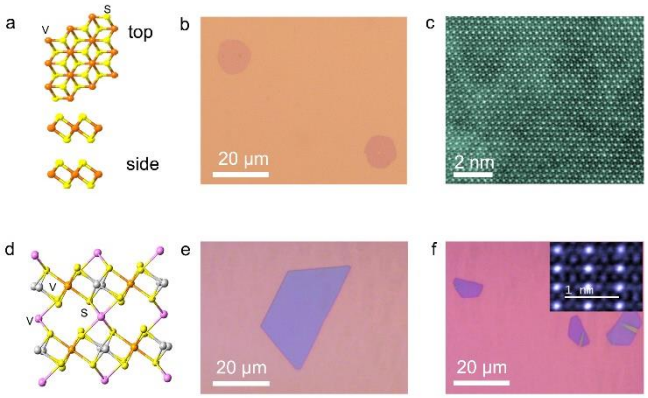

Figure | S3. Optical image and structure of VS_2 and V_5S_8. a. top and side view of VS_2. b. Optical image of VS_2. c. STEM image of few layer VS_2. d, Crystal structure of V_5S_8, e and f, Optical images of V_5S_8 and the inset of (f) shows the corresponding STEM image.

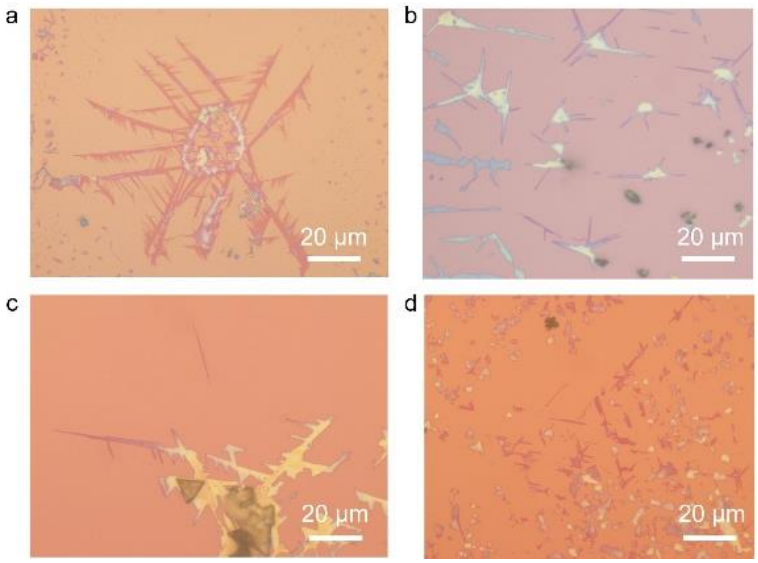

Figure | S4. The yield of the superlattice phase obtained with almost same growth conditions. All the samples are the superlattices.

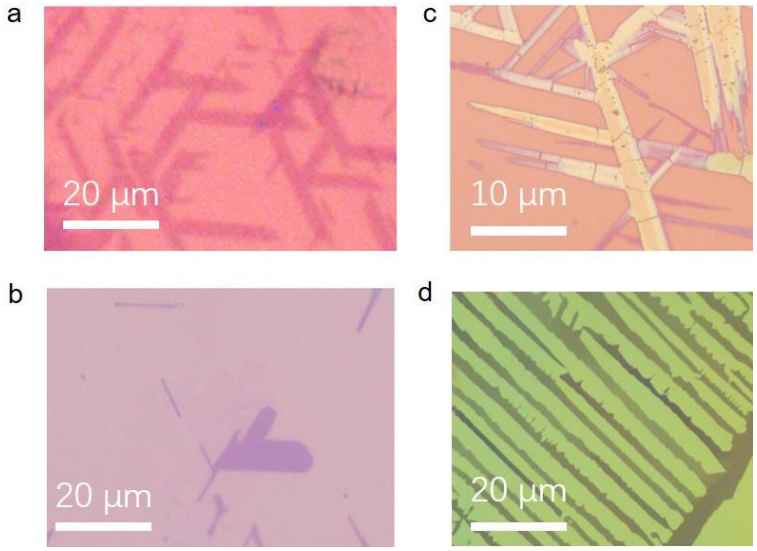

Figure | S5. Optical images of VS_2-VS superlattice with different shapes. (a, b and c) The VS_2-VS superlattices with different thickness and (d) the array of the superlattices.

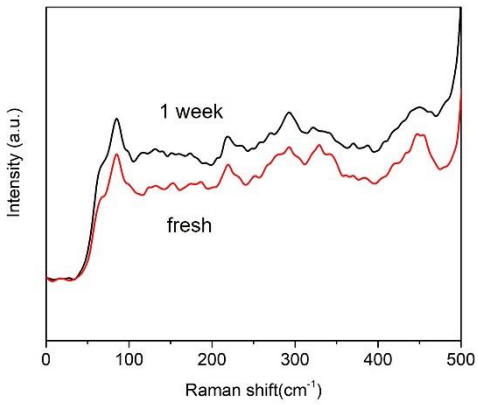

Figure | S6. Raman spectrum of VS_2-VS before and after device measurement, illustrating no structure change of VS_2-VS.

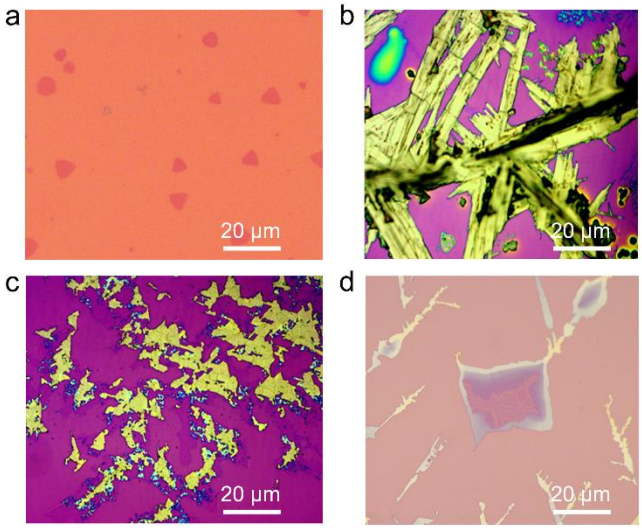

Figure | S7. The superlattice will be decomposed with excessive sulfur supplement.

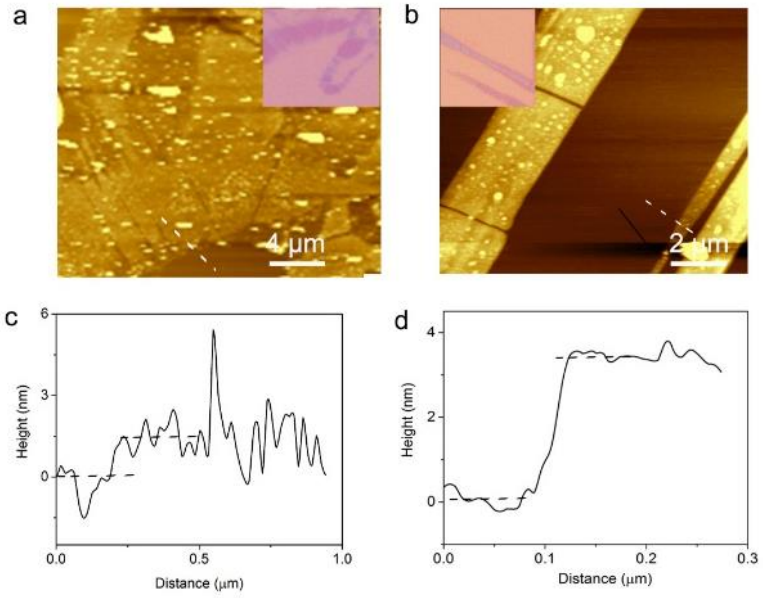

Figure | S8. AFM images of VS_2-VS superlattice. (a) and (c), the thickness of 1.5 nm can be considered as the monolayer of VS_2-VS. (b) and (d), the thickness of few-layer VS_2-VS. The corresponding atomic structure is shown in Fig. 2.

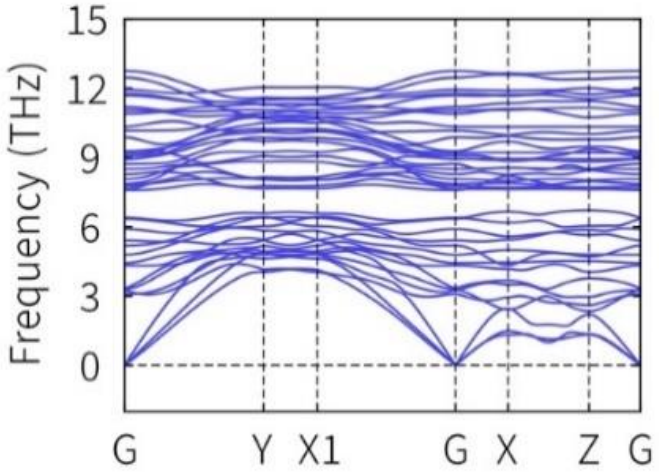

Figure | S9. Phonon spectrum of VS_2-VS superlattice in AFM-4 state.

Table S3. Calculated Raman modes.

Band	$\nu(\mathrm{cm}^{-1})$	Band	$\nu(\mathrm{cm}^{-1})$	Band	$\nu(\mathrm{cm}^{-1})$
5	**108 (90)**	16	253	28	309

6	110	17	255	29	**329 (345)**
8	144	19	262	32	363
9	148	22	283	34	373
11	173	23	291	35	390
14	**212 (223)**	25	298	37	**398 (455)**

Symmetry allowed Raman modes extracted from the calculated phonon spectrum (see Fig. S9). The comparison between calculation results and experimentally observed main peaks (in bracket) are highlighted using bold text. In order to understand the nature of the phonon modes of this new material, we carried out DFT calculations of the phonon spectrum based on the crystal structure presented in the SI (Fig. S3d). The calculated result could well capture the energies of active Raman modes and reveal the nature of each Raman mode accessed in our experiment, as listed in Table S3. It is worth noting that the discrepancy of the energies of Raman peaks between the calculated one and the experimental results probably stems from the intermediate correlation of V atoms that leads to difficulty to accurately evaluate the dielectric tensor and force parameters in DFT calculations of the phonon spectrum of VS_2-VS superlattice.

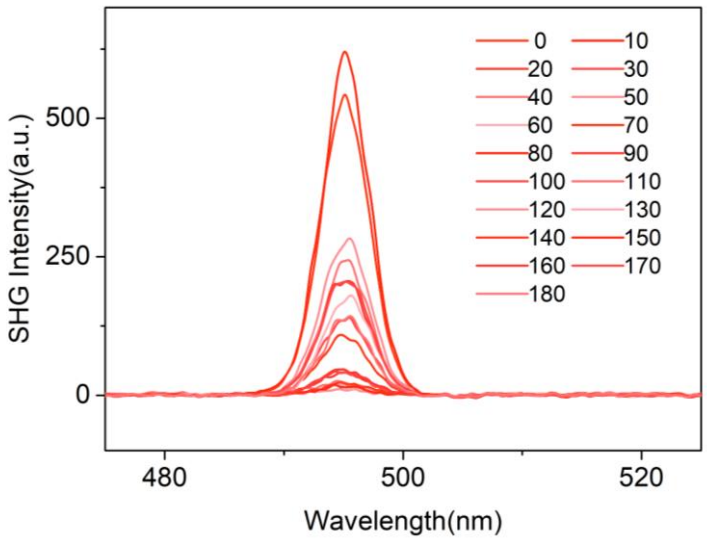

Figure | S10. SHG intensity of VS_2-VS superlattice dependency on the azimuthal

angle.

Since the observed SHG signal in VS_2-VS superlattice is very weak, it might be attributed to the following reasons: (1) The imperfection of the surface terminal of the VS_2-VS superlattice together with the different environments near the interface may lead to the interfacial inversion symmetry breaking, allowing for a SHG signal. (2) A strong coupling between the thin sample and substrate could lead to some distortions in samples that lowers the symmetry and facilitates the appearance of SHG signal.

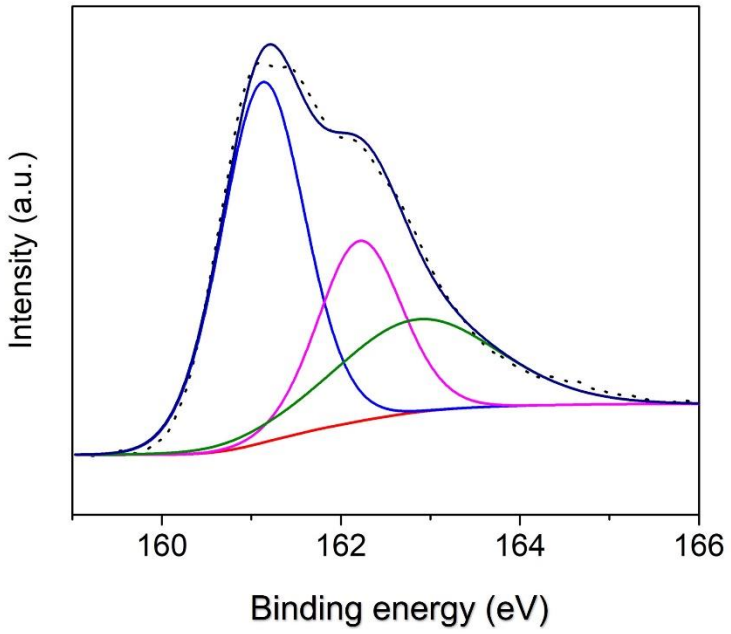

Figure | S11. XPS analysis of VS_2-VS superlattice. XPS spectra of S element in VS_2-VS superlattice. The peaks locating at 161 eV and 162.3 eV are the S $2p_{3/2}$ and S $2p_{1/2}$. The peak locating at high energy is attributed to the oxidized superlattice.

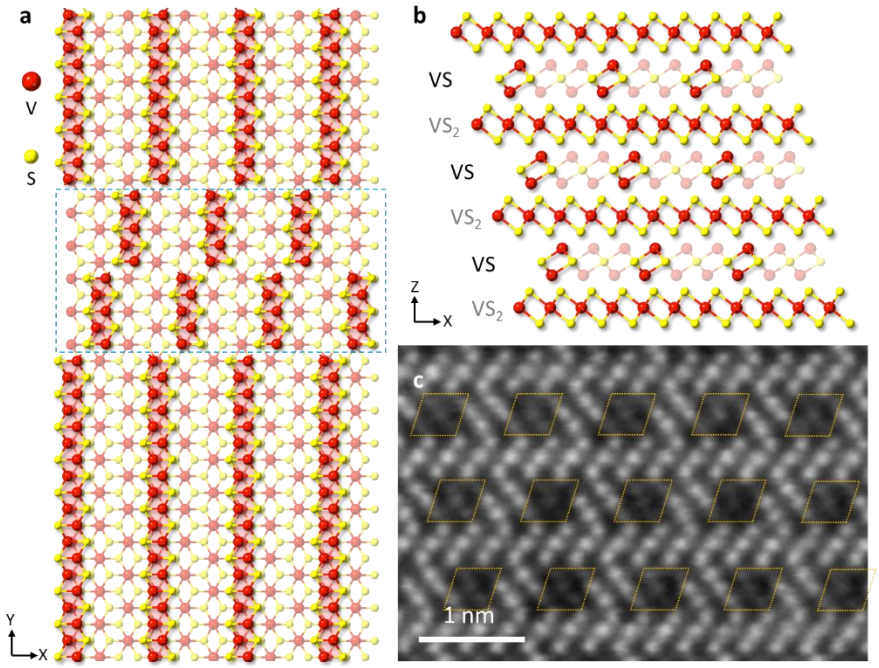

Figure S12 | VS_2-VS superlattice with short segments of displaced 1D-VS chains. Atomic model from the top view (a) and from side view (b). (c) Cross section STEM-ADF image of the VS_2-VS superlattice identical to Fig. 2d. The short segments of displaced 1D-VS chains contribute to weaker ADF contrast of in the VS planes highlighted by orange-dotted rhombus.

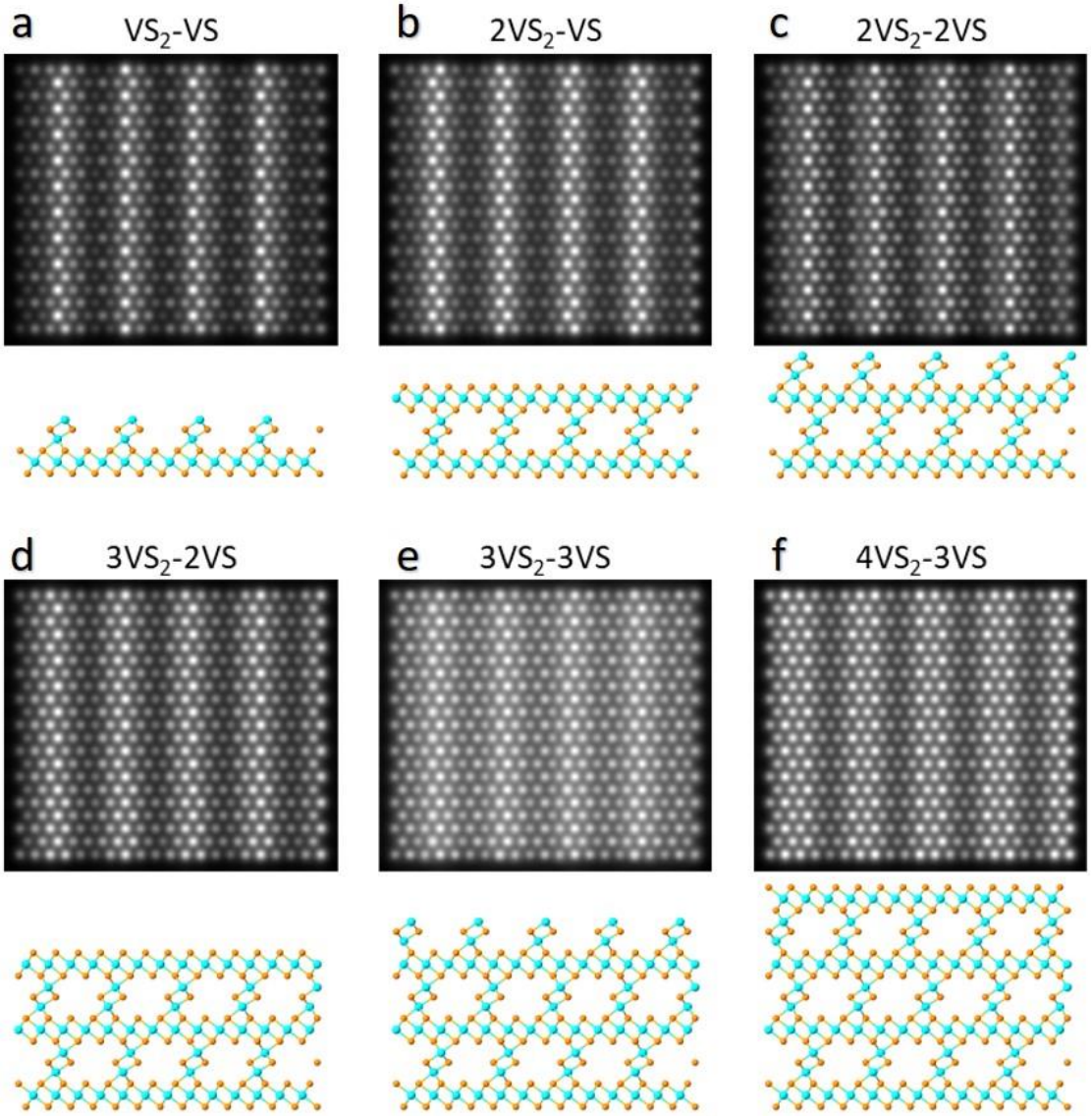

Figure | S13. The atomic structures of VS_2-VS superlattice. (a)-(f) STEM simulations (top-view) and the corresponding atomic models (side-view) of VS_2-VS, $2VS_2$-VS, $2VS_2$-2VS, $3VS_2$-2VS, $3VS_2$-3VS, and $4VS_2$-3VS, respectively.

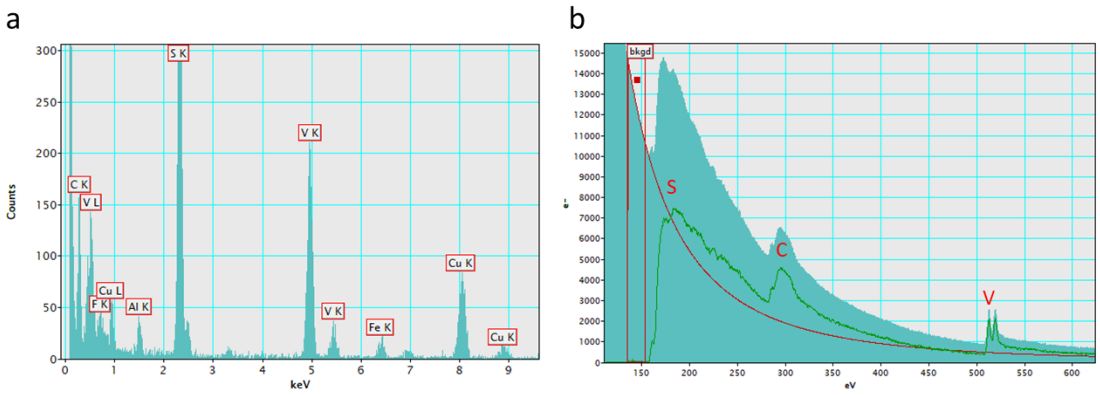

Figure | S14. (a) EDS and (b) EELS spectrum of the VS_2-VS layer. No potassium and iodine signals were detected within the e-beam scanning area (~100 x 100 nm^2).

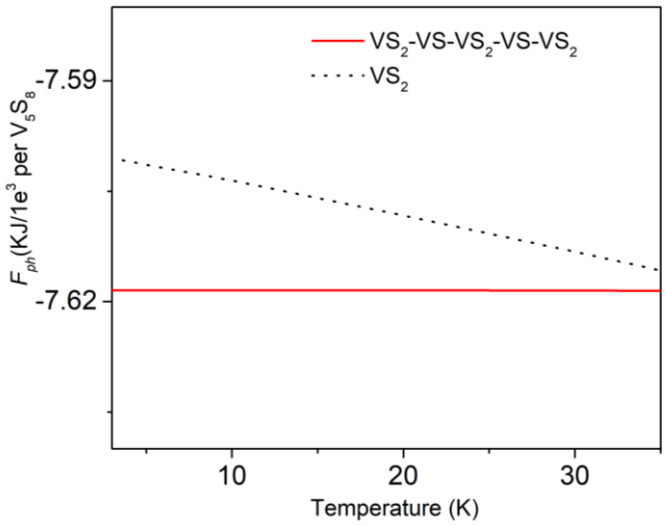

Figure | S15. Helmholtz free energy of VS_2-VS superlattice and VS_2.

The free energy $F(T)$ of the chemical reaction ($5VS_2 + 2H_2 = [VS_2\text{-}VS\text{-}VS_2\text{-}VS\text{-}VS_2] + 2H_2S$) in different temperatures are shown in Fig. S15, where the free energy is approximated by the sum of electronic internal energy $U_{el}(T = 0)$ and phonon Helmholtz free energy $F_{ph}(T)$, i.e., $F(T) \approx U_{el}(T = 0) + F_{ph}(T)$ [17].

Section II: Symmetry analysis of IPHE

In this section, we would discuss the symmetry requirements of IPHE in VS_2-VS superlattice. The relevant symmetry is the mirror reflection symmetry about a plane that is perpendicular to the Hall plane. This is because the Hall conductance vanishes once the system obeys such a symmetry[18]. For example, consider an IPHE measurement setup, in which the electrical current **j**, the electric field **E,** and the magnetic field **B** are all in the xy plane. Assuming the electric field is in the x direction, the Hall effect is expressed as $j_y = \sigma_{yx}E_x$. A mirror reflection about the xz plane, $\mathcal{M}_y$, reverses the sign of y while keeping the sign of x ($x \to x, y \to -y$). As a result, the Hall response equation becomes $j_y = -\sigma_{yx}E_x$. Thus, σ_{yx} has to be zero if the system is invariant under $\mathcal{M}_y$. As a pseudovector, an in-plane magnetization **m** breaks this mirror symmetry in general and the Hall effect survives, except in the case of **m** being parallel to the mirror plane. Interestingly, if there are two mirror planes perpendicular to each other in crystal, one can see that the system with an arbitrary in-plane **m** is invariant under a joint symmetry of $\mathcal{M}_x \otimes \mathcal{M}_y \otimes \mathcal{T}$ ($x \to -x, y \to -y, t \to -t$), where t is time and $\mathcal{T}$ represents time reversal operation. The Hall response equation under this joint symmetry operation again becomes $j_y = -\sigma_{yx}E_x$ and thus the Hall vanishes. We want to emphasize that the only assumption made here is within the linear response region, $j_y \propto E_x$. In our new structure of VS_2-VS superlattice, there is only one mirror plane, $\mathcal{M}_y$. When the magnetization is not parallel to this plane, $\mathcal{M}_y$ remains, which is in excellent agreement with a zero Hall resistivity observed in our experiment for $B \,||\, y$.

Section III: Onsager reciprocal relations

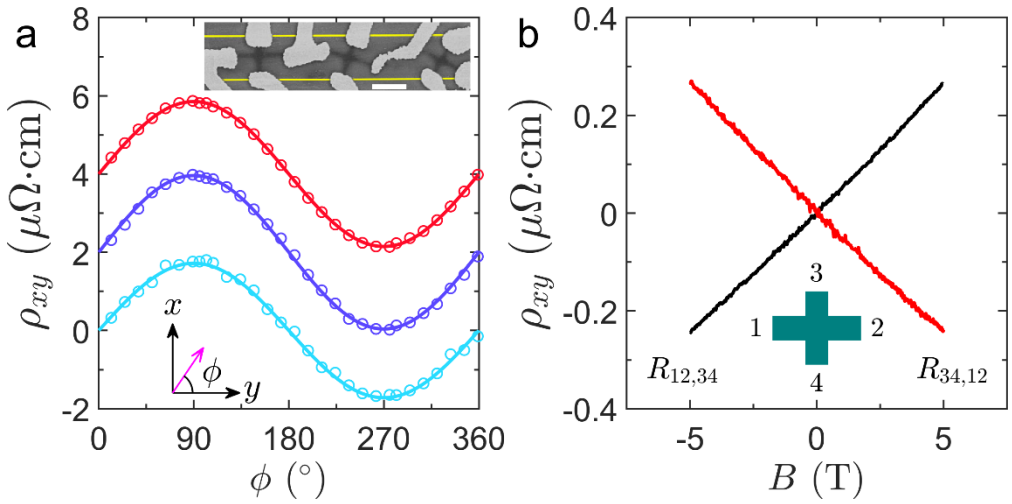

Figure | S16. Dependence of the in-plane Hall on the direction of the electrical current. (a) IPHE of S14 as a function of the magnetic field angle at T = 30 K and B = 9 T. Three curves represent three directions of the current, 0, 20, 40 degrees with respect to the y axis (the horizontal direction). Data are vertically shifted for clarity. The inset is an SEM image of three devices. Two yellow lines mark the outline of the original sample before patterning. The scale bar is 2 μm. (b) Field dependence of IPHE for S22 at T = 30 K. Two measurements were done by interchanging the current and the voltage electrodes, denoted as $R_{12,34}(B)$, solid black line and $R_{34,12}(B)$, solid red line. Here, $R_{12,34}$ represents the Hall measurement by injecting the current from 1 to 2 (parallel to the long axis of 1D chains) and measuring the voltage between 3 and 4 (perpendicular to the 1D chains). The signals satisfy the Onsager reciprocal relations, $R_{12,34}(B) = R_{34,12}(-B)$.

We have prepared Hall bars along different crystalline directions, as shown in the top inset of Fig. S16(a). Consequently, the current in different Hall bars will be along different directions. Surprisingly, the field angular dependence for these devices shows

no phase shift, indicating that IPHE is independent of the current direction. In particular, even when the current is parallel to the field, IPHE is not zero so long as the field is not along the y axis. At first glance, this may look counter-intuitive, but we are going to show that it is actually in accordance with the so-called Onsager reciprocal relations. As for the off-diagonal elements in the resistivity tensor, the relations state that $\rho_{xy}(B) = \rho_{yx}(-B)$. By interchanging the current and voltage electrodes, both $\rho_{xy}(B)$ and $\rho_{yx}(B)$ were measured, as depicted in Fig. S16(b). As expected, $\rho_{xy}(B) = \rho_{yx}(-B)$ is satisfied within experimental error. By further considering that the Hall effect is anti-symmetric in B, i.e., $\rho_{xy}(-B) = -\rho_{xy}(B)$, the reciprocal relations can be rewritten to $\rho_{xy}(B) = -\rho_{yx}(B) = \rho_{y\bar{x}}(B)$. Here, $\bar{x}$ denotes the negative direction of the x axis. One immediately recognizes that $\rho_{y\bar{x}}(B)$ corresponds $\rho_{xy}(B)$ being rotated by 90 degrees counterclockwise. Note that the field is not rotated. Since the analysis is only based on the Onsager reciprocal relations, we conclude that IPHE is invariant under $4n$-fold rotation of the current direction, regardless of the crystal symmetry. Here, n is a natural number. In the linear response region, $j_x = \sigma_{xy}E_y$, $4n$-fold symmetry implies an isotropic response. This is indeed what we observed, i.e., IPHE being independent of the current direction. In sharp contrast, the planar Hall effect is determined by the angle between the current and the field.

Section IV: Magnetoresistance

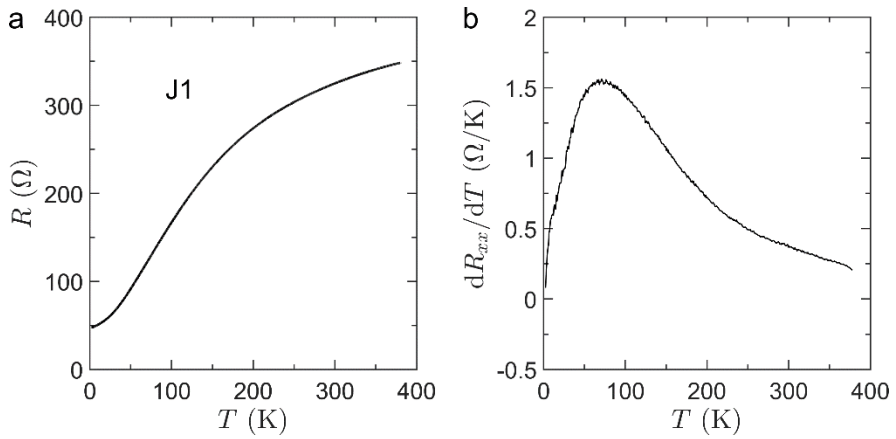

Figure | S17. Temperature dependence of the resistance of J1 and its derivative.

V_5S_8 is known to be an antiferromagnetic metal with a monoclinic structure. It is basically VS_2 layered structure intercalated with V atoms (we use VS_2-V to denote this structure). These intercalated V atoms have magnetic moments, which align antiferromagnetically. As another phase of V_5S_8, the superlattice VS_2-VS consists of VS_2 layers intercalated with VS chains. The chemical states of V atoms between layers are apparently different in two phases. In VS_2-V system [19], it was found that the valence of V is V^{3+} and V^{4+}, while it is V^{2+} and V^{4+} in VS_2-VS, according to the XPS and EELS data shown in the main text (Fig.1e and Fig. 3). It is reasonable to believe that the chemical state leads to different magnetic states of V atoms and different band structures. Consequently, two phases exhibit different properties. VS_2-V shows antiferromagnetism with a Neel temperature of 32 K. Its magnetoresistance and Hall display a jump at 3.5 T, signaling a spin-flop transition[20]. The low critical field of the transition indicates a relatively low magnetrocrystalline anisotropy. On the other hand, the temperature dependence of resistivity in VS_2-VS is smooth below 380 K. In Fig. S17, both the resistance and its derivative are smooth from 1.9 K to 380 K. All of our

measured samples show no sign of a kink in resistance versus temperature curves, which indicates no phase transition. The linear magnetoresistance and Hall up to 9 T suggest no spin-flop transition. Given the mild magnetocrystalline anisotropy that 3d electrons can provide, this result highly suggests the absence of antiferromagnetism in VS_2-VS superstructure.

The temperature dependence of resistivity of a metal is usually linear when the temperature is not very low, because of the electron-phonon scattering. The resistivity of our samples displays a broad hump feature if the linear background is removed. The maximum appears at about 200 K, which coincides with the temperature at which the Hall coefficient changes its sign, as seen in Fig. S22. The change of the sign is most likely due to a parallel conduction of multiple bands at the Fermi energy, confirmed by our theoretical calculations, as shown in Fig. S29. Thus, the deviation from the linear behavior could be related to a multi-band effect. On the other hand, similar deviation has also been observed in other transition metal compounds and various mechanisms have been proposed[21]. Currently, it is difficult to pin down the mechanism. Nevertheless, there is no indication that the temperature anomaly is related to the IPHE.

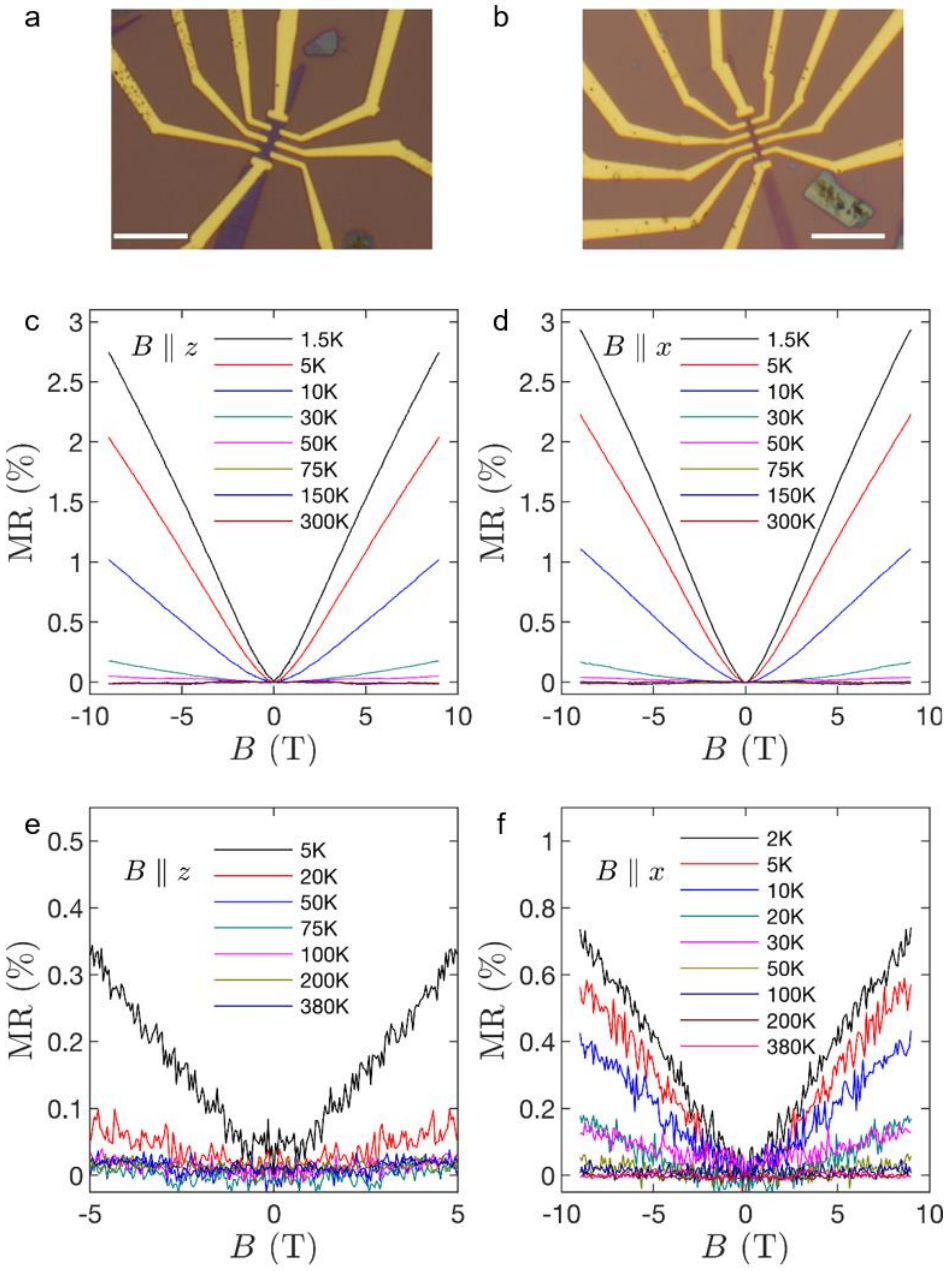

Figure | S18. Magnetoresistance of S18 and S20 at several temperatures. (a and b) Optical images of S18 and S20. The scale bars represent 10 μm. (c and d) Magnetoresistance of S20. (e and f) Magnetoresistance of S18. (c and e) The field is parallel to z axis. (d and f) The field is parallel to x axis. All curves are symmetrized.

Figure S18 shows two samples S18 and S20. Measured by atomic force microscope, their thicknesses are 18 nm and 5.5 nm, respectively. Their magnetoresistance (MR) are

calculated as [$R(B)$-$R(0)$]/$R(0)$. MR is small even at low temperatures. Above 50 K, it is negligible. The MR is marginal, of the order of 1 % at 9 T. It displays a non-saturating dependence. It is known that open orbits can give rise to a non-saturating MR. Such an MR is expected to exhibit a strong anisotropy with respect to the field orientation, as open cyclotron orbits can only appear when the field orientation is in certain range. The MR of our samples depends weakly on the field orientation, see Fig. S18 (c and d). Thus, the MR is unlikely due to anisotropic Fermi surface. The more or less isotropic MR suggests a spin-related origin. However, further study is needed to pinpoint the mechanism. The magnitude of MR in S20 is much larger than that in S18. Note that the residue resistivity ratios of S18 and S20 are 3,1 and 1.1, respectively. The significant difference in the sample quality may explain the difference in MR, as MR often depends on the carrier density and scattering.

Section V: Absence of long-range magnetic order

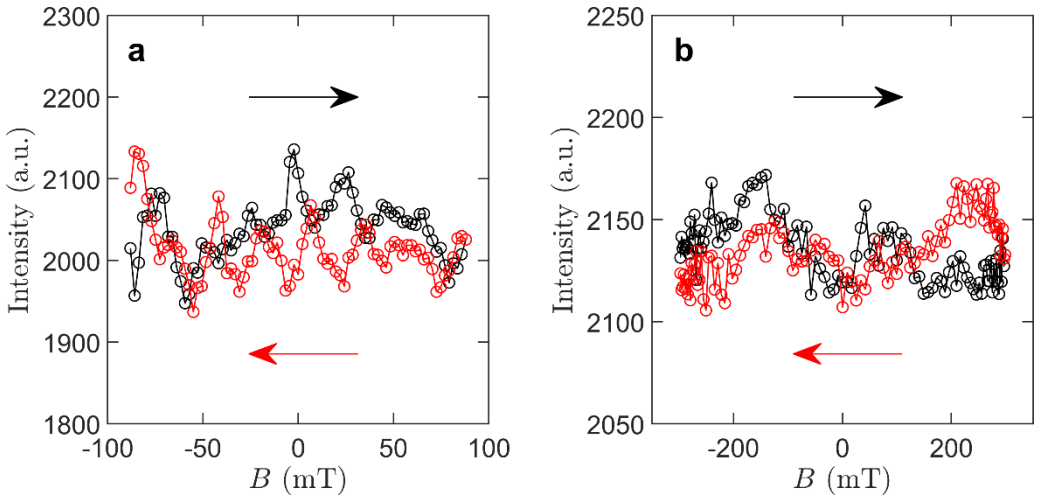

Figure | S19. Magneto-optical Kerr effect. Samples were measured at T = 100 K, with a) an out-of-plane and b) an in-plane applied field. Arrows represent the scanning directions.

The Kerr effect of several samples has been investigated by Kerr microscope. Typical signals plotted in Fig. S19 are the average gray level of selected regions at each field. A background consisting of quadratic and linear term has been removed, due to Faraday effect and time-related drift, respectively. Both in-plane and out-of-plane field were applied at 100 K. In all cases, no recognizable hysteresis loop has been observed. As the hysteresis loop is a characteristic of ferromagnetic materials, this result confirms the absence of ferromagnetic order. MOKE is usually believed to be insensitive to antiferromagnetic order. Recently, it has been demonstrated that in special cases, MOKE can probe antiferromagnetism[22]. Our MOKE results show no indication of antiferromagnetism, although we cannot conclusively exclude such a possibility.

Section VI: Temperature and field-angle dependence of IPHE

Over 20 samples have been measured, with thicknesses ranging from 4 to 70 nm. IPHE were observed in all samples. Figure S20 shows the optical images of another two samples S12 and S16 with different thicknesses. S12 is about 8 nm thick and S16 is around 70 nm thick. The temperature dependence of resistance is smooth down to the lowest measured temperature. In Figure S21, both samples display a marked IPHE. The in-plane Hall conductance versus temperature are plotted in semi-log graphs to emphasize the exponential decay with temperature. The thinnest sample we have measured is 4 nm thick. Since thin and thick (~70 nm) films exhibit similar IPHE, we conclude that it is a bulk effect and has nothing to do with surfaces.

Figure S22 shows the temperature dependence of both IPHE and OPHE. At all

temperatures, their field dependence is linear. Shown in Figure S22(c), IPHE and OPHE generally decrease with temperature. However, OPHE displays a much stronger temperature dependence at low temperatures and reverses its sign at 165 K. The in-plane and out-of-plane Hall conductivity are calculated by $\sigma_{xy} \approx \rho_{xy}/\rho^2_{xx}$. The former one is monotonic with respect to temperature, while the latter one is not. The different behaviors of two Hall effects reflect their distinctive origins. Figure S23 shows the transport of device J2. Both the IPHE and OPHE display a linear field dependence. The OPHE changes sign at 150 K. The in-plane Hall conductivity exhibits an exponential decay with temperature, yielding a gap about ~ 6.1 meV.

Figure S24 shows the angular dependence of IPHE and OPHE. The behavior is highly similar to the one in Figure 4. Figure S25 shows the 3D plots of the Hall resistivity. Based on data presented in the main text, the full angular dependence of the Hall effect is sketched in a polar diagram. When the field rotates in three principal planes, the Hall resistivity follows a sine/cosine function. Therefore, the shape of the angular dependence is a sphere.

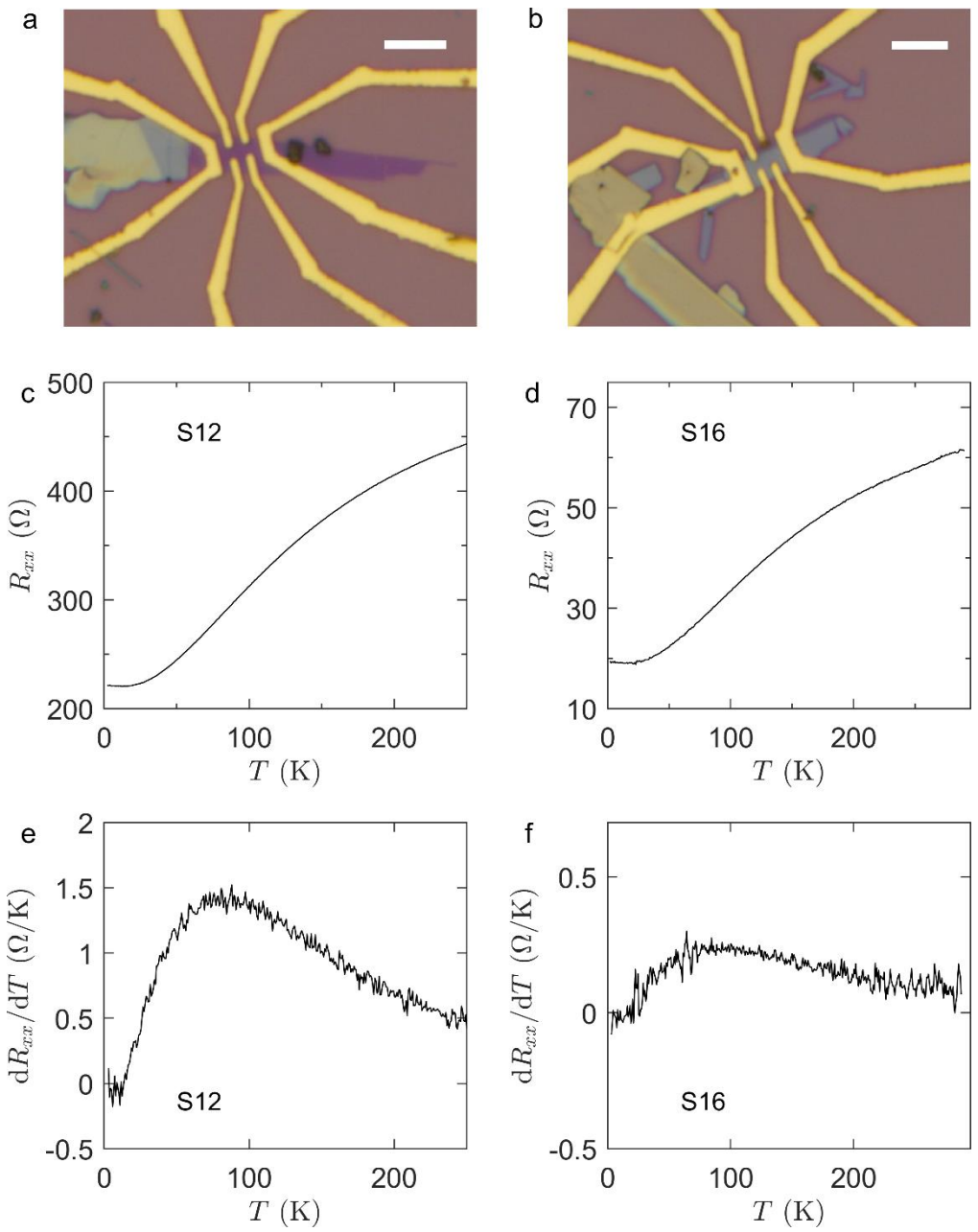

Figure | S20. Temperature dependence of resistance of S12 and S16. (a and b) The optical images of two samples. The scale bars are 5 μm. One of the contacts in (b) is broken, but the remaining contacts are enough for a standard four-point measurement of resistance and Hall. (c and d) Temperature dependence of resistance. (e and f) Derivative of the resistance. No apparent kink can be recognized.

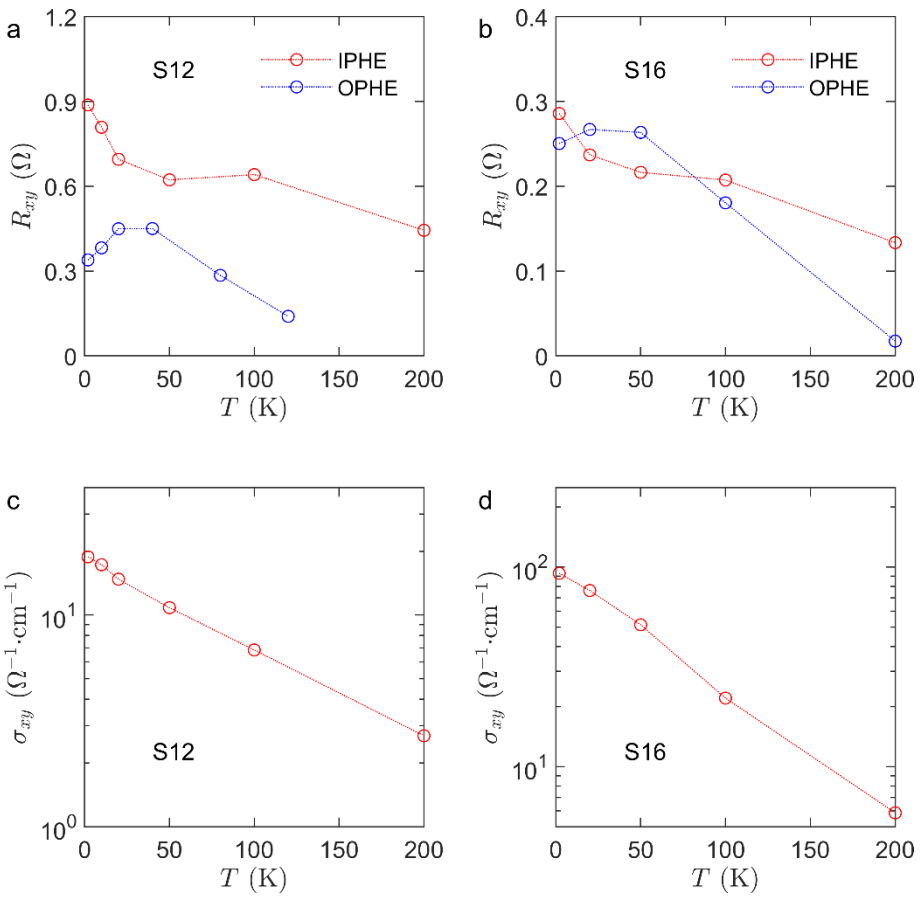

Figure | S21. Temperature dependence of the Hall effect of S12 and S16. (a and b) The Hall resistance at 9 Tesla versus temperature. (c and d) The Hall conductivity versus temperature.

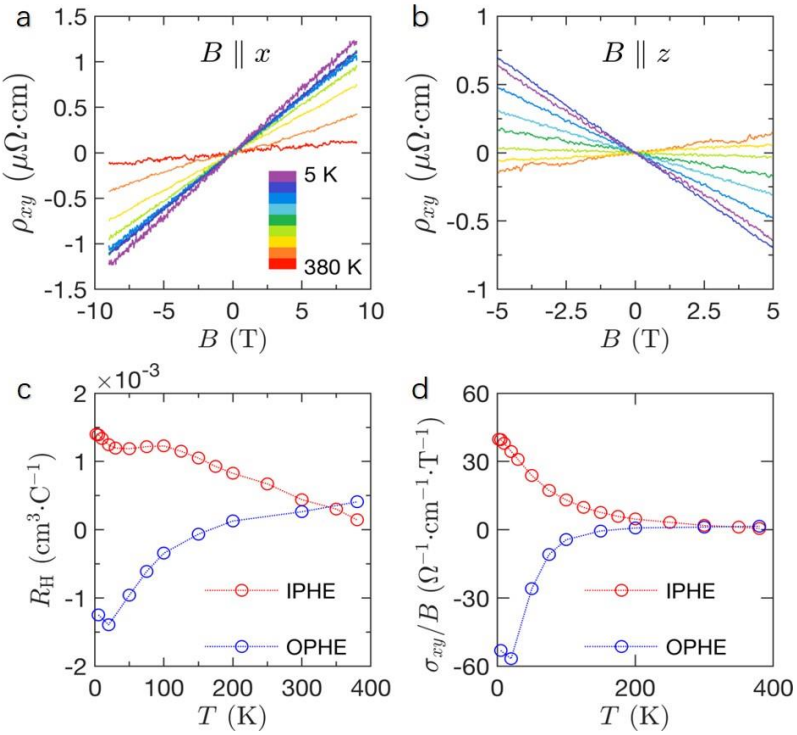

Figure | S22. Temperature dependence of the Hall resistivity for S18. (a) Field dependence of IPHE at different temperatures. (b) Field dependence of OPHE at different temperatures. For clarity, not all data are shown. (c) The Hall coefficients versus temperature. Even at room temperature, the in-plane Hall coefficient is larger than the out-of-plane one. (d) The in-plane and out-of-plane Hall conductivity versus temperature.

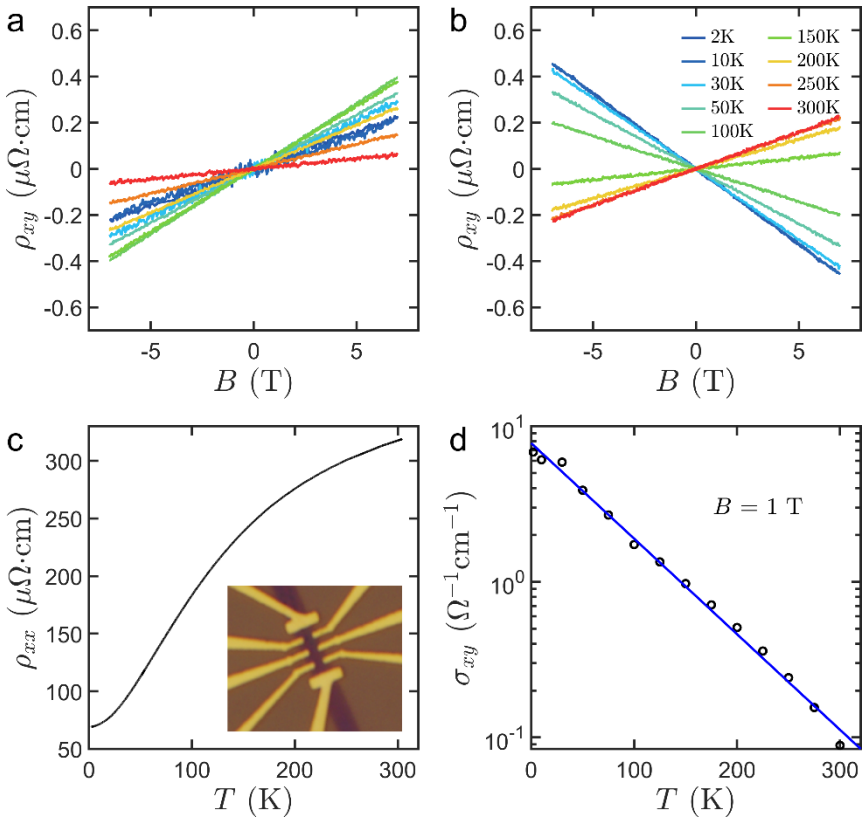

Figure | S23. Hall effects and resistivity of J2. (a) IPHE. (b) OPHE. (c) Temperature dependence of the resistivity. The inset is the optical image of the device (d) The Hall conductivity versus temperature at 1 T. The blue line is a linear fit.

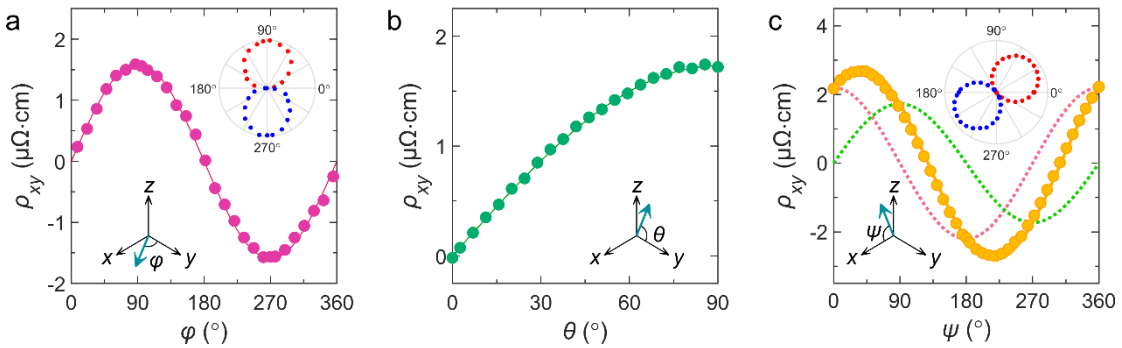

Figure | S24. Angular dependence of the Hall resistivity for S18 at *B* = 9 T. Solid lines in (a) and (b) represent fits to sine functions. The data in (c) can be decomposed

as the sum (solid yellow line) of the in-plane component (cosine, dashed red line) and the out-of-plane component (sine, dashed green line). The insets in (a) and (c) show the angular dependence in a polar diagram. Red/blue color represent the positive/negative sign of the Hall resistivity, while the radius represents the absolute value. Data in (a) are measured at 5 K, while those in (b) and (c) are measured at 100 K.

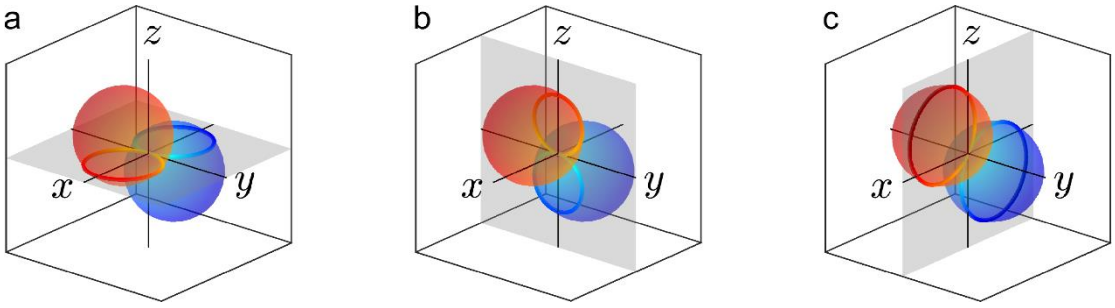

Figure | S25. Magnetic field angular dependence of the Hall resistivity at B = 7 T. (a, b, c) Schematic 3D illustration of the angular dependence of the Hall resistivity in a polar diagram, corresponding to the data from Fig. 4 in the main text. Red/blue color represents the positive/negative sign of the Hall resistivity, while the radius represents the absolute value. The principal planes are shaded in gray. The solid lines represent the intersection between the Hall surface and the principal planes, corresponding to the polar diagram in the top insets of Fig. 4**d**, **e**, **f** in the main text.

Section VII: DFT calculations methods and results

Calculation methods:

The electronic structures of the VS_2-VS were performed in VASP package[23] using PAW[24] pseudopotentials with $3s^2 3p^6 3d^3 4s^2$ and $3s^2 3p^4$ valence electron configurations for V atoms and S atoms correspondingly. The electron exchange-correlation part was described with the generalized gradient approximation (GGA)[25] in the scheme of PBE

functional[26]. The plane-wave cutoff energy was set to be 400 eV and the convergence thresholds for electronic and ionic relaxations were chosen to be 1.0×10^{-8} eV and 0.001 eV/Å. A $4 \times 14 \times 4$ (conventional cell) and $8 \times 8 \times 8$ (primitive cell) Γ-centered *k*-point mesh with Gaussian smearing of width 0.2 eV was used to perform Brillouin zone integrations. The spin-orbital coupling (SOC) effect was taken into account in the non-colinear magnetic calculations. The Dudarev *et al.*'s approach[27] was used to treat localized *d* orbitals of V atoms with the rotationally invariant effective $U = 3.0$ eV. The phonon calculations were performed in a $1 \times 4 \times 1$ supercell with respect to the conventional cell. The in-plane Hall effect (IPHE) calculations were performed based on Wannier tight-binding models, which were constructed using WANNIER90 code[28] with the *d* orbitals in V atoms and *p* orbitals in S atoms as the initial guess of local basis.

Calculation results:

Based on experimental atomic structure analysis using annular dark-field scanning transmission electron microscopy (ADF-STEM) and the cross-section TEM, the crystal structure formed by 2D VS_2 and 1D VS chain array is constructed. The VS-VS_2 structure (Fig. S26) belongs to the *C2/m* space group generated by lattice translation, inversion symmetry *P*, mirror M_y, and translational symmetry $t = \left\{1|\frac{\boldsymbol{a}}{2}, \frac{\boldsymbol{b}}{2}, 0\right\}$. The primitive and conventional cells with experimental lattice constants are used for DFT calculations, as shown in Fig. S26.

To study the magnetic ground states of the VS-VS_2 system, we have performed DFT calculations using an exhaustive method. As the magnetization is mainly located at the V site, within the primitive cell (Fig. S26a), there are sixteen possible magnetic

configurations in total (labeled as FM-#) with ten independent states, as shown in Fig. S27. To further make comparison with antiferromagnetic (AFM) states, we extend our DFT calculation to conventional cell (Fig. S26b) that has even number of V atoms to satisfy collinear AFM state. To keep a relatively high symmetry of the system, e.g., inversion symmetry and M_y symmetry, we limit our AFM calculations to six independent configurations (labeled as AFM-#) that all has the C_{2y}=P*M_y symmetry, as shown in Fig. S28. The total energy of all these different magnetic configurations is summarized in Table. S4. Among these FM and AFM states, the AFM-4 has the lowest energy.

We further calculated the magnetic anisotropy energy of the system, which shows a very small magnetic anisotropy with the energy of magnetization along the *y* direction slightly lower (0.16 meV per V atom) than that of the *x*/*z* direction, suggesting a small spin-orbit coupling effect and soft magnetic behavior. Furthermore, we calculated its phonon spectrum as shown in Fig. S9, which does not have imaginary vibrational frequencies, confirming the stability of this magnetic configuration of the VS_2-VS superlattice. We note that the energy difference between AFM and FM states is quite small, which could potentially lead to strong magnetic fluctuation. This is consistent with experimental results that show the absence of detectable long-range magnetic ordering. Thus, we use the AFM-4 state for the following calculations of band structure, Berry curvature and intrinsic anomalous Hall conductivity.

Table S4. Relative energies with respect to the total energy of the ground state AFM-

4 [in unit of eV per superlattice (VS_2-VS-VS_2-VS-VS_2)]. The equivalent configurations are highlighted by bold text.

Magnetic configuration	ΔE	Magnetic configuration	ΔE	Magnetic configuration	ΔE
FM-1	0.2494	FM-9	0.1423	AFM-1	0.1000
FM-2	0.2645	FM-10	0.1664	AFM-2	0.0923
FM-3	0.0267	FM-11	0.3161	AFM-3	0.2394
FM-4	0.1898	**FM-12 (FM-10)**	**0.1664**	AFM-4	0
FM-5 (FM-2)	**0.2645**	FM-13	0.0934	AFM-5	0.2395
FM-6	0.0995	**FM-14 (FM-11)**	**0.3161**	AFM-6	0.1364
FM-7 (FM-4)	**0.1898**	**FM-15 (FM-13)**	**0.0934**		
FM-8	0.1422	**FM-16 (FM-9)**	**0.1423**		

In the absence of the external magnetic field, the AFM state is colinear with P and $\tilde{T}$ symmetry, where $\tilde{T} = \left\{T|\frac{\boldsymbol{a}}{2},\frac{\boldsymbol{b}}{2},0\right\}$. In this case, the band structure is double-degenerate, and the Berry curvature vanishes in the entire Brillouin zone (BZ), resulting in zero intrinsic AHC. In the presence of the external magnetic field $\boldsymbol{B}$, the local magnetic moment from V atoms tilts, leading to a net magnetization along $\boldsymbol{B}$ that breaks the $P\tilde{T}$ symmetry. The double-degenerate band is split by the exchange field accordingly. It is important to note that when $\boldsymbol{B}||y$, the system can always be viewed as an AFM state with its magnetization aligning in the xz plane plus an FM state aligning along the y direction. Both of these two parts have glide mirror symmetry $\widetilde{M}_y = \left\{M_y|\frac{\boldsymbol{a}}{2},\frac{\boldsymbol{b}}{2},0\right\}$ that constrains zero AHC, i.e., $\sigma_{xy}(B||y) = 0$. For the other cases, there can exist nonzero intrinsic AHC, i.e., an in-plane magnetization can yield an out-of-plane AHE. Our calculation based on the AFM-4 further confirms such symmetry analysis and shows zero AHC

when $\boldsymbol{B}||y$ and nonzero AHC when $\boldsymbol{B}||x/z$. We note that though the AFM-4 state only represents one possible magnetic ground state, but the unconventional AHC behavior based on our symmetry analysis should be appliable to the other possible magnetic configurations.

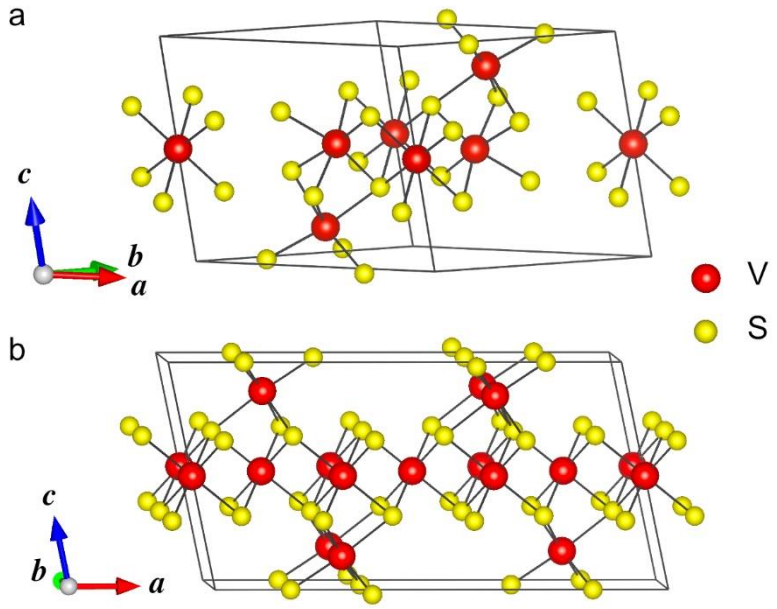

Figure | S26. (a) Primitive cell and (b) conventional cell of the VS_2-VS structure.

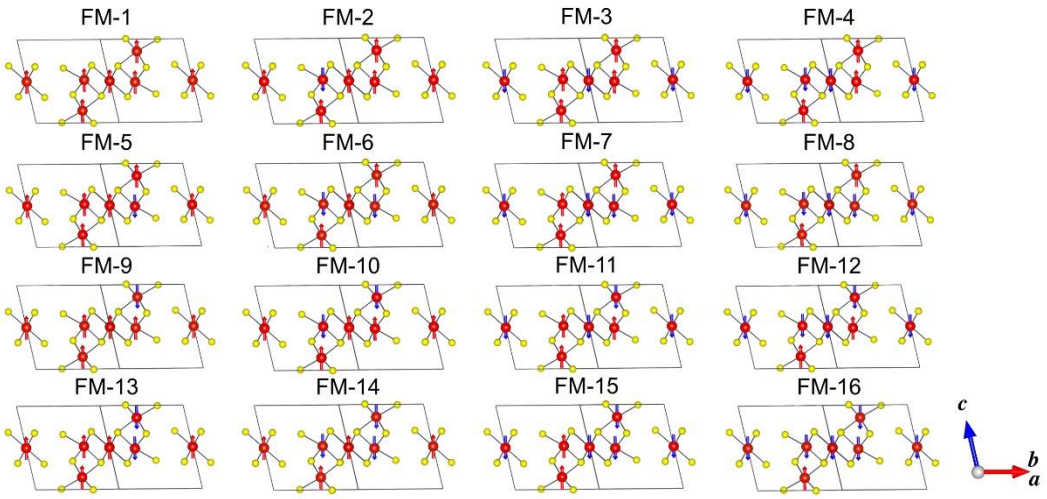

Figure | S27. Possible collinear magnetic configurations in the primitive cell. The red and blue arrows in V atoms indicate opposite directions of the local magnetic moment.

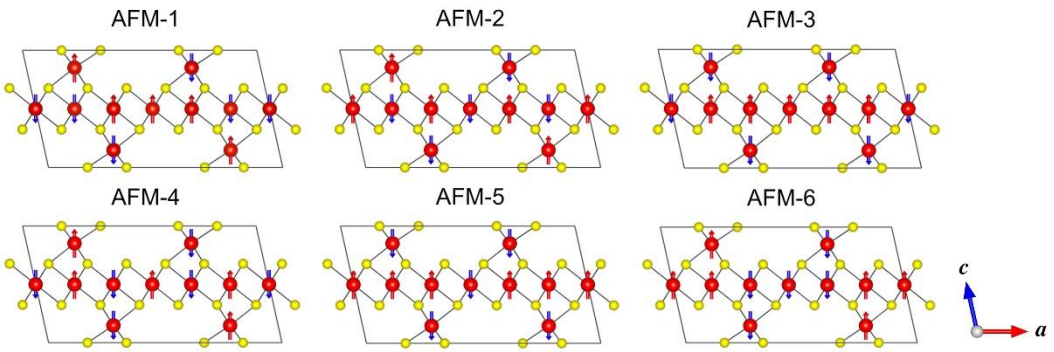

Figure | S28. Possible antiferromagnetic magnetic configurations in the conventional cell. The red and blue arrows in V atoms indicate opposite directions of the local magnetic moment.

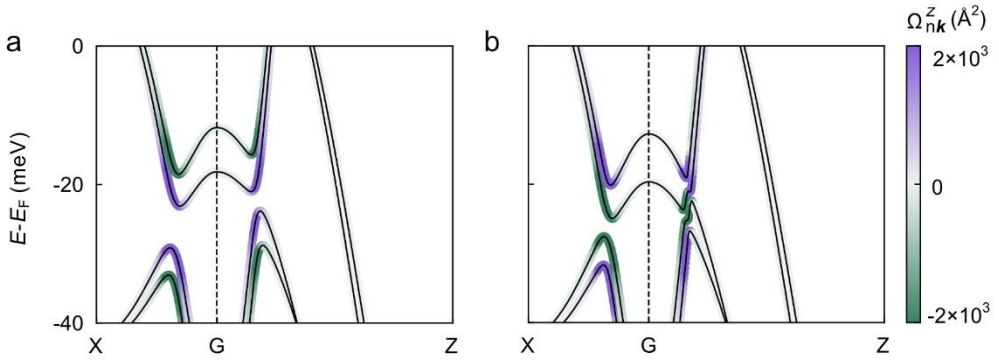

Figure | S29. Band resolved berry curvature distribution. The band structure of AFM-4 with a net magnetization ($0.42\mu_B$) (a) along the *x* and (b) *z* direction to simulate the spin canting effect induced by the external magnetic field ***B***. The spin-orbital

coupling effect is taken into account. Due to the spin canting effect, a net magnetization raised along $\boldsymbol{B}$, which breaks the $P\tilde{T}$ symmetry and splits the double-degenerate band (gapped nodal line). The large Berry curvature Ω_n^z is mainly distributed near the band splitting region, as highlighted by green and purple color in (a) and (b). This field-induced Berry curvature is responsible for the intrinsic IPHE discussed in the main text.

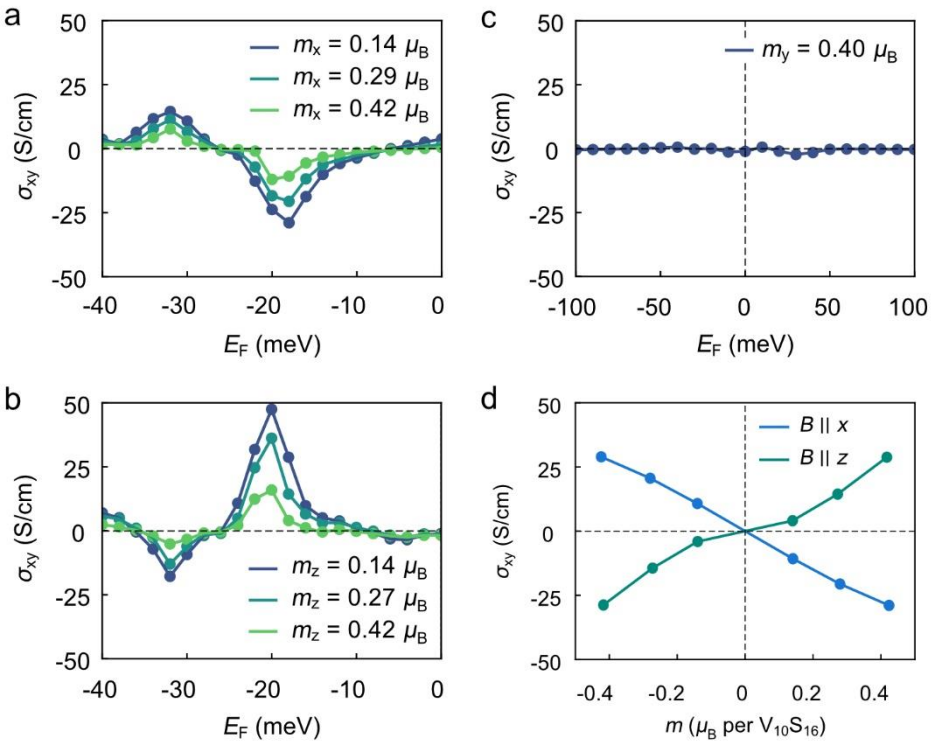

Figure | S30. The calculated intrinsic AHC with different m to mimic the change of magnitude of magnetic fields for (a) in-plane with $\boldsymbol{B}$||x and (b) out-of-plane with B||z, where m is the total magnetization in the $V_{10}S_{16}$ conventional cell in unit of μ_B. The AHC peak happens in the band splitting region, which is consistent with the calculated band structure (see Fig.S30). (c) In-plane AHC with B||y. (d) The in-plane and out-of-plane AHC versus m induced by the external magnetic field.

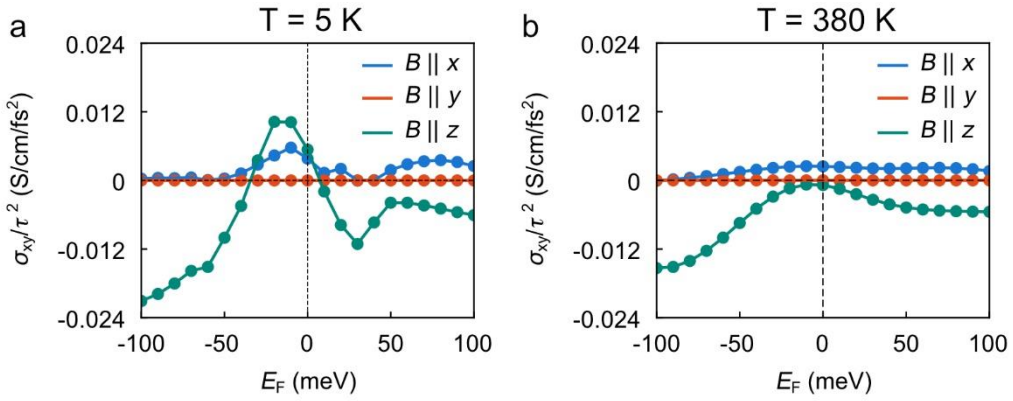

Figure | S31. The calculated ordinary Hall conductivity due to the anisotropic Fermi surface. (a) and (b) show the DFT calculation of the ordinary Hall conductivity for the magnetic field along different directions at 5K and 380 K, respectively.

Section VIII: Difference between IPHE and Planar Hall effect

In the linear response region, the Onsager reciprocal relations pose strict constraints on the resistivity tensor: $\rho_{ij} = \rho_{ji}$. When the time reversal symmetry (TRS) is broken, the relations become $\rho_{ij}(B) = \rho_{ji}(-B)$, where $\boldsymbol{B}$ represents all TRS breaking fields, i.e., magnetic field B and magnetization M. On the other hand, the resistivity tensor can be decomposed into a symmetric and an antisymmetric pair:

$$\rho_{ij} = \frac{\rho_{ij} + \rho_{ji}}{2} + \frac{\rho_{ij} - \rho_{ji}}{2} \equiv \rho_{ij}^{S} + \rho_{ij}^{A}$$

Applying the Onsager reciprocal relations $\rho_{ij}(B) = \rho_{ji}(-B)$ to the tensor yields:

$$\begin{cases} \rho_{ij}^{S}(B) = \rho_{ij}^{S}(-B) \\ \rho_{ij}^{A}(B) = -\rho_{ij}^{A}(-B) \end{cases}$$

The B-symmetric planar Hall effect (PHE) follows $\rho_{ij}^{S}(B) = \rho_{ij}^{S}(-B)$ [29]and the B-

antisymmetric PHE follows $\rho_{ij}^{S}(B,M) = \rho_{ij}^{S}(-B,-M) = -\rho_{ij}^{S}(-B,M) = -\rho_{ij}^{S}(B,-M)$[30,31]. Both are the off-diagonal element of the symmetric tensor, hence essentially anisotropic MR. In contrast, the OPHE and IPHE is the antisymmetric tensor satisfying $\rho_{ij}^{A}(B) = -\rho_{ij}^{A}(-B)$. It can be seen that $E_i = \rho_{ij}^{A}(B)J_j$ respects TRS if the time reversal operation is also applied to the field ($B \to -B$), which means that the IPHE is a dissipationless effect, just like the OPHE and the normal anomalous Hall effect.

Section IX: IPHE due to the anisotropic Fermi surface

we calculated the ordinary Hall conductivity (OHC) due to the Lorentz force based on the DFT calculations of band structures via the formula (see Section 12.5 in Ref[32])

$$\sigma^{xy}(\boldsymbol{B}) = -\frac{e^3\tau^2}{\hbar}\int \frac{d\boldsymbol{k}}{(2\pi)^3} v_x (\boldsymbol{v_k} \times \boldsymbol{B}) \cdot \nabla_{\boldsymbol{k}} v_y \frac{\partial f_0}{\partial \varepsilon}$$

The calculated results are given in Fig. S31. We found that the anisotropic Fermi surface indeed leads to nonzero Hall conductivity for the magnetic field ***B*** along the x or z direction but zero Hall conductivity for the ***B*** along the y direction.

Several key features of our observed IPHE are **inconsistent** with the above fermi surface anisotropy mechanism. First, the temperature dependences of the IPHE and OPHE are distinctive. The OPHE changes sign around 150 K, while the IPHE remains positive up to 380 K. Secondly, the Fermi surface anisotropy mechanism implies that the OPHE should be much larger than the IPHE, since our VS_2-VS superlattices have an intercalated structure, the in-plane mobility is expected to be much higher than the out-of-plane one. However, this is not in line with our experimental results of the VS_2-VS superlattice that shows even smaller OPHE than the IPHE. Thirdly, the IPHE occurred in 4 nm thick flakes, where the orbital effect of the in-plane magnetic field is

strongly suppressed due to confinement. Thus, the IPHE cannot be solely explained by the Fermi surface anisotropy mechanism.

Reference:

1 Ji, Q. *et al.* Metallic Vanadium Disulfide Nanosheets as a Platform Material for Multifunctional Electrode Applications. *Nano Lett* **17**, 4908-4916 (2017).

2 Hochbaum, A. I., Fan, R., He, R. & Yang, P. Controlled growth of Si nanowire arrays for device integration. *Nano Lett* **5**, 457-460 (2005).

3 Li, S. *et al.* Vapour-liquid-solid growth of monolayer MoS_2 nanoribbons. *Nat Mater* **17**, 535-542 (2018).

4 Hardy, W. J. *et al.* Thickness-Dependent and Magnetic-Field-Driven Suppression of Antiferromagnetic Order in Thin V_5S_8 Single Crystals. *ACS Nano* **10**, 5941-5946 (2016).

5 Zhao, D. *et al.* Observation of unconventional anomalous Hall effect in epitaxial CrTe thin films. *Nano Research* **11**, 3116-3121 (2018).

6 Wen, Y. *et al.* Tunable Room-Temperature Ferromagnetism in Two-Dimensional Cr2Te3. *Nano Lett* **20**, 3130-3139 (2020).

7 Chua, R. *et al.* Room Temperature Ferromagnetism of Monolayer Chromium Telluride with Perpendicular Magnetic Anisotropy. *Adv Mater* **33**, e2103360 (2021).

8 Coughlin, A. L. *et al.* Van der Waals Superstructure and Twisting in Self-Intercalated Magnet with Near Room-Temperature Perpendicular Ferromagnetism. *Nano Lett* **21**, 9517-9525 (2021).

9 Nabei, Y. *et al.* Current-induced bulk magnetization of a chiral crystal CrNb3S6. *Applied Physics Letters* **117** (2020).

10 Yang, J. *et al.* Ultrahigh-current-density niobium disulfide catalysts for hydrogen evolution. *Nat Mater* **18**, 1309-1314 (2019).

11 Moh, G. H. Mutual Pb2+/Sn2+ substitution in sulfosalts. *Mineralogy and Petrology* **36**, 191-204 (1987).

12 Esaki, L. & Chang, L. L. New Transport Phenomenon in a Semiconductor "Superlattice". *Physical Review Letters* **33**, 495-498 (1974).

13 Zhao, Y. *et al.* Crossover from 3D to 2D quantum transport in Bi2Se3/In2Se3 superlattices. *Nano Lett* **14**, 5244-5249 (2014).

14 Li, X.-B., Chen, N.-K., Wang, X.-P. & Sun, H.-B. Phase-Change Superlattice Materials toward Low Power Consumption and High Density Data Storage: Microscopic Picture, Working Principles, and Optimization. *Advanced Functional Materials* **28** (2018).

15 Falmbigl, M., Alemayehu, M. B., Merrill, D. R., Beekman, M. & Johnson, D. C. In-plane structure of ferecrystalline compounds. *Crystal Research and Technology* **50**, 464-472 (2015).

16 Devarakonda, A. *et al.* Clean 2D superconductivity in a bulk van der Waals superlattice. *Science* **370**, 231-236 (2020).

17 Togo, A. & Tanaka, I. First principles phonon calculations in materials science. *Scripta*

Materialia **108**, 1-5 (2015).

18 Liu, X., Hsu, H. C. & Liu, C. X. In-plane magnetization-induced quantum anomalous Hall effect. *Phys Rev Lett* **111**, 086802 (2013).

19 Fujimori, A., Saeki, M. & Nozaki, H. Electron correlation,d-band formation, and magnetism inV5S8: Photoemission-spectroscopy study. *Physical Review B* **44**, 163-169 (1991).

20 Niu, J. *et al.* Anomalous Hall effect and magnetic orderings in nanothick V5S8. *Physical Review B* **96** (2017).

21 Gunnarsson, O., Calandra, M. & Han, J. E. Colloquium: Saturation of electrical resistivity. *Reviews of Modern Physics* **75**, 1085-1099 (2003).

22 Higo, T. *et al.* Large magneto-optical Kerr effect and imaging of magnetic octupole domains in an antiferromagnetic metal. *Nat Photonics* **12**, 73-78 (2018).

23 Kresse, G. & Hafner, J. Ab initio molecular dynamics for liquid metals. *Phys Rev B Condens Matter* **47**, 558-561 (1993).

24 Blochl, P. E. Projector augmented-wave method. *Phys Rev B Condens Matter* **50**, 17953-17979 (1994).

25 Perdew, J. P. *et al.* Atoms, molecules, solids, and surfaces: Applications of the generalized gradient approximation for exchange and correlation. *Phys Rev B Condens Matter* **46**, 6671-6687 (1992).

26 Perdew, J. P., Burke, K. & Ernzerhof, M. Generalized Gradient Approximation Made Simple. *Phys Rev Lett* **77**, 3865-3868 (1996).

27 Dudarev, S. L., Botton, G. A., Savrasov, S. Y., Humphreys, C. J. & Sutton, A. P. Electron-energy-loss spectra and the structural stability of nickel oxide: An LSDA+U study. *Physical Review B* **57**, 1505-1509 (1998).

28 Mostofi, A. A. *et al.* An updated version of wannier90: A tool for obtaining maximally-localised Wannier functions. *Computer Physics Communications* **185**, 2309-2310 (2014).

29 Liang, S. *et al.* Experimental Tests of the Chiral Anomaly Magnetoresistance in the Dirac-Weyl Semimetals Na3Bi and GdPtBi. *Physical Review X* **8** (2018).

30 Wang, Y. *et al.* Antisymmetric linear magnetoresistance and the planar Hall effect. *Nature Communications* **11** (2020).

31 Jiang, B. *et al.* Chirality-Dependent Hall Effect and Antisymmetric Magnetoresistance in a Magnetic Weyl Semimetal. *Physical Review Letters* **126** (2021).

32 Ziman, J. M. Electrons and Phonons, Oxford at the Clarendon Press